Research Article

Superior strength-ductility combination resulted from hetero-zone boundary affected region in Cu-Fe layered material

Hao Ran [a], Peihao Ye [a], Fengjiao Guo [a], Mingsai Wang [a], Wuli Su [a], Xue Chen [a], Si Gao [b], Nobuhiro Tsuji [b,c], Yuntian Zhu [d], Xiaochong Lu [a,*], Chongxiang Huang [a,e,*]

[a] *School of Aeronautics and Astronautics, Sichuan University, Chengdu 610065, China*
[b] *Department of Materials Science and Engineering, Kyoto University, Yoshida Honmachi, Sakyo-ku, Kyoto 606-8501, Japan*
[c] *Elements Strategy Initiative for Structural Materials (ESISM), Kyoto University, Yoshida Honmachi, Sakyo-ku, Kyoto 606-8501, Japan*
[d] *Department of Materials Science and Engineering, City University of Hong Kong, Hong Kong, China*
[e] *Failure Mechanics and Engineering Disaster Prevention and Mitigation Key Laboratory of Sichuan Province, Sichuan University, Chengdu 610065, China*

A B S T R A C T

The hetero-zone boundary affected region (HBAR) significantly influences the mechanical behaviors of layered materials, where the deformation mechanisms differ from those in the bulk layers. In this study, three kinds of heterogeneous Cu-Fe layered materials with different interface spacing but identical total thicknesses were prepared. The effects of HBAR and strain partitioning on the tensile behavior of the layered materials were investigated. The results showed that layered materials had enhanced yield strength and uniform elongation with decreasing interface spacing. During tensile deformation, geometrically necessary dislocations (GNDs) were generated at hetero-zone boundaries and piled up near them, resulting in hetero-deformation induced (HDI) strengthening and HDI work hardening. Surface profilometry measurements showed that the Cu and Fe layers exhibited obvious strain partitioning and mutual constraint. With decreasing interface spacing, strain partitioning is enhanced by interlayer constraint, which prevented strain localization at interfaces and thus improved the synergetic deformation of layers. A higher fraction of HBAR can improve the mechanical performance of heterogeneous layered materials. This study deepens our understanding of the relationship between HBAR and strength-ductility synergy and provides some insight into the design of layered materials.

© 2023 Published by Elsevier Ltd on behalf of The editorial office of Journal of Materials Science & Technology.

1. Introduction

Strength and ductility are key mechanical properties of structural materials but often exhibit a trade-off relationship. For instance, nano-grained materials can achieve high strength, however, their limited strain-hardening capacity leads to low ductility. Recently, hetero-structured (HS) materials have emerged as a promising class of materials that can overcome this dilemma and achieve a better combination of strength and ductility [1–9]. HS materials are composed of heterogeneous zones with distinct microstructural and mechanical characteristics [10–13]. These HS materials include gradient [1–8], bimodal [9,14,15], lamellar [16,17], harmonic [18,19], hierarchical fibrous-grained [20], and layered [21–25] materials.

Layered materials are particularly suitable for fundamental studies since they have well-defined interfaces between layers [13]. For example, Ma et al. [24] fabricated three kinds of Cu-CuZn layered materials with different interface spacings, and they found that both strength and ductility increased with decreasing interface spacing. Huang et al. [25] prepared a layered material with alternating fine-grained Ti and coarse-grained (CG) Al layers and observed that its ductility surpassed that of both Ti and Al standalone layers. The enhanced mechanical properties are attributed to the synergistic interaction between the mechanically incompatible layers [26,27]. During deformation, the heterogeneity between layers induces mutual constraint and strain gradient near interfaces. The strain gradient is accommodated by geometrically necessary dislocations (GNDs) that accumulate near interfaces, thus generating hetero-deformation induced (HDI) stresses and forest hardening to strengthen and toughen the material. Strain partitioning occurs si-

multaneously, which produces HDI work hardening and enhances ductility [17,22,28–30].

Hence, the interface is crucial for improving the mechanical properties of layered materials. In our previous work, the strain distribution and evolution near the interface were characterized using a high-resolution digital image correlation analysis technique [31]. A hetero-zone boundary-affected region (HBAR) with constant-width zone with a negative strain gradient was observed and initially named as interface-affected zone (IAZ), which originates from dislocations accumulated at the interface and coordinates the inter-zone deformation heterogeneity. Moreover, an optimal interface spacing for superior mechanical properties of layered materials was discovered. However, the formation mechanism of HBAR and its effect on the deformation behaviors of layered materials remain unclear. This is crucial for designing layered materials with superior mechanical properties.

In this work, we prepare three HS Cu-Fe layered materials with different interface spacing by accumulative roll bonding (ARB) and annealing treatment to investigate the above issues. There is no element diffusion between Cu and Fe layers, which allows for a more accurate analysis of the effects of interfacial strain gradient and GNDs on the material's properties, without being influenced by intermetallic compounds. Cu and Fe are low-cost and extensively used in engineering applications, offering significant potential for industrial production. We investigate the distribution and variation of GND density to analyze the formation and evolution of HBAR. The lateral surface height profiles are measured to study the synergetic deformation behaviors and strain partitioning with decreasing interface spacing. Finally, the effect of HBAR volume fraction on strengthening is discussed.

2. Experimental procedure

2.1. Material preparation

Commercial pure Cu (99.9 wt%) and pure Fe (99.8 wt%) sheets were used to prepare Cu-Fe layered materials using the ARB technique. Before the ARB process, the surfaces of individual sheet were cleaned with acetone and then brushed to remove the oxide layer. These treatments ensured uniform surface roughness and strong bonding strength. Subsequently, two treated sheets were stacked and roll-bonded at room temperature using a two-high rolling mill at a nominal thickness reduction of 50% per cycle. The first ARB cycle was performed on a stacking sequence of "Cu (0.5 mm)-Fe (1 mm)-Cu (0.5 mm)" which can effectively prevent the severe bending of the sheet during rolling when using a "Cu (1 mm)-Fe (1 mm)" stacking sequence. Because of such stacking sequence, the bonding in the following ARB cycles only occurred between two Cu layers and the thicknesses of the top and bottom Cu layers were always half of the inner layers. After roll-bonding, the material was cooled in air and halved before performing the next cycle. After the second ARB cycle, annealing at 650 °C for 5 min followed by water cooling was performed between each ARB cycle to prevent the shear bands that could be otherwise formed during rolling because of the large hardness difference between the Fe and Cu layers. After 2, 4, and 6 cycles, the total thickness are all 1 mm, and layer numbers were 5, 17, and 65, respectively. After the ARB process, both Cu and Fe layers are elongated grains, as shown in the optical micrograph in Fig. S1(a) in the Supplementary Material. The ARB-processed samples were then annealed at 300 °C for 2 h in a vacuum tube furnace. This annealing temperature exceeds the recrystallization temperature of Cu but remains lower than that of Fe, which is supported by the hardness variation of the Cu and Fe layers in Fig. S1(b). The samples were labeled as A5, A17, and A65, respectively.

2.2. Mechanical tests

The microhardness distribution across the interface was measured using a 25 g load with a 15 s dwell time. Five independent measurements were performed for each sample to ensure reproducibility. Uniaxial tensile tests were carried out on a Shimadzu AG-100 KN machine at a strain rate of 5×10^{-4} s^{-1}, using samples with a gage size of 8 mm × 2 mm × 1 mm. A clip-on extensometer was attached to monitor the strain during testing. At least three specimens were tested for each condition to verify the experimental reliability.

2.3. Microstructure characterization

The cross-sectional microstructures of HS Cu-Fe layered material before and after tension were examined by transmission electron microscopy (TEM) and scanning electron microscopy (SEM) with electron backscattering diffraction (EBSD). The TEM observation was conducted on an FEI Tecnai G2 T20 microscope operating at 200 kV. The EBSD analysis was conducted at an accelerating voltage of 15 kV with a step size of 50 nm. The height contours on the lateral surface of after-tensile samples were measured by a Bruker Contour-I white light interferometer in a vertical scanning mode.

3. Results

3.1. Heterogenous microstructures

Fig. 1(a–c) presents optical images of layered samples with various layer numbers but similar total thickness. The average interface spacing of A5, A17, and A65 samples is approximately 250, 65, and 16 μm, respectively. The Cu and Fe layers, represented by orange and gray, exhibit good bonding without delamination. Microhardness distributions are shown in Fig. 1(d–f). The Fe layers display a hardness of ∼2.1 GPa, while Cu layers possess a relatively low hardness of ∼0.9 GPa. The layer interfaces are denoted by dotted lines, based on the periodic distribution of hardness value. Apart from the hardness distribution, similar textures were found across three samples, as shown in Fig. S2. Fig. 1(g) presents an EBSD phase map illustrating the microstructure of the A65 sample. The Cu layer has a face-centered cubic (FCC) structure, and the Fe layer has a body-centered cubic (BCC) structure. Thus, the interface between two phases is distinct, this type of interface (FCC/BCC) exhibits a diverse range of variations in grain size, grain orientation, phase structure, and other characteristics, which is different from other types of interface [23–25] and may have good impact on mechanical properties. After undergoing ARB and annealing processes, the layered samples demonstrate CG Cu and elongated-grained (EG) Fe layers. It means that the Cu layer underwent recrystallization, while the Fe layer only recovered during annealing.

TEM observations were performed on the A65 sample to investigate the microstructure of HS Cu-Fe layered material before tensile deformation. Fig. 2(a) exhibits a microstructure transient from the CG Cu layer to the EG Fe layer. No obvious interfacial reaction is detected. The corresponding EDS mapping further confirms the sharp Cu-Fe interface without any noticeable chemical element diffusion (Fig. 2(b)). The high-resolution TEM (HRTEM) images in Fig. 2(b) reveal the crystal structure of Cu and Fe, respectively. These findings collectively suggest an excellent bonding in the Cu-Fe layered sample, enabling us to study the interface-strengthening effect without interfering with other factors. The detailed microstructures of individual Cu and Fe layers are displayed in Fig. 2(c–f). As expected, the Cu layer has undergone recrystallization, forming equiaxed grains with an average size of 10.8 μm (Fig. 2(c, e)). The corresponding selected area electron diffraction
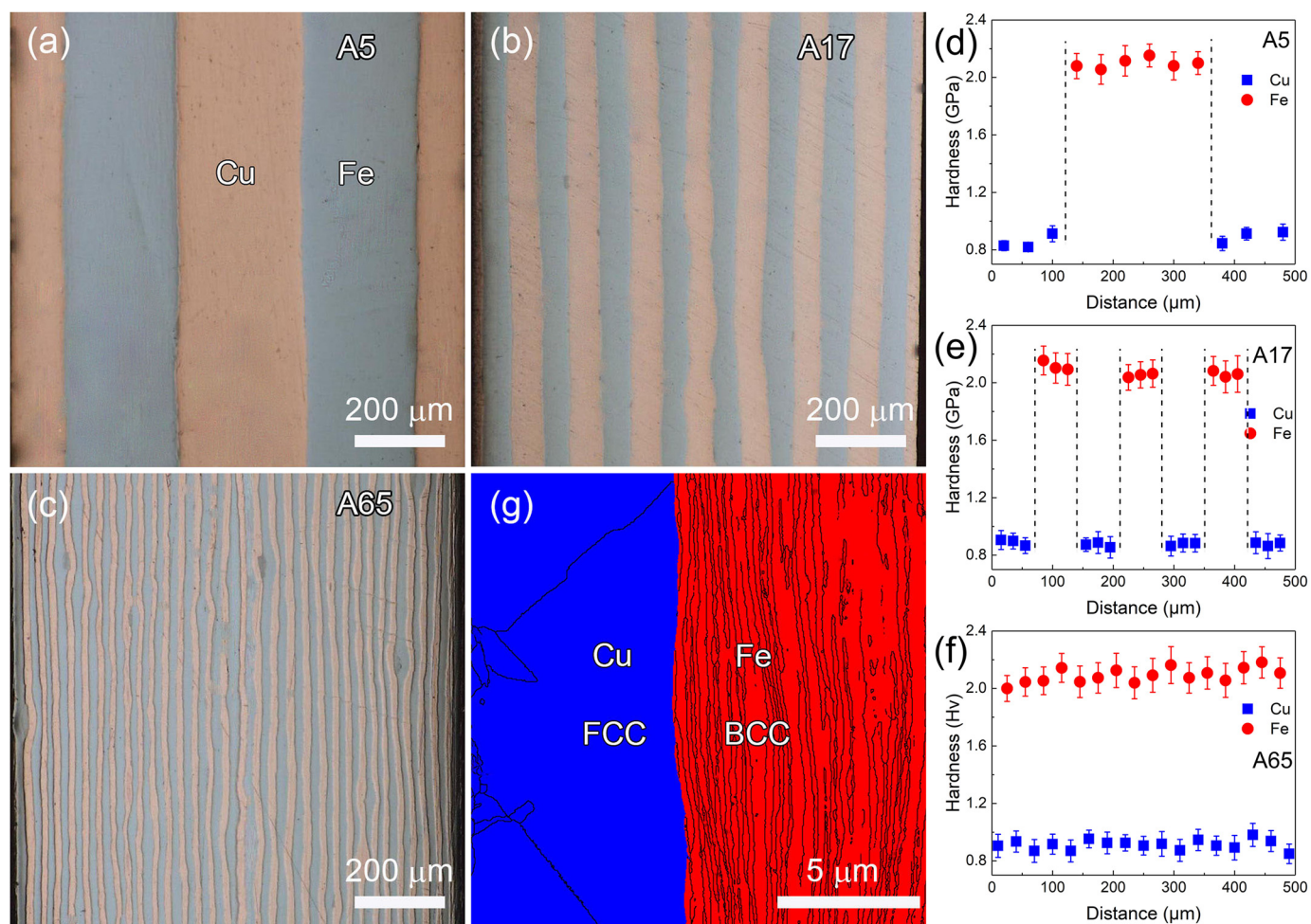
Fig. 1. Optical micrographs and corresponding microhardness distributions of (a, d) A5, (b, e) A17 and (c, f) A65 sample. (g) EBSD phase map showing the microstructure across the interface of the A65 sample.

(SAED) pattern indicates the presence of annealing twins. Conversely, Fig. 2(d, f) shows that the Fe layer has elongated grains with an average layer thickness of 0.13 μm and a high density of dislocations. This high dislocation density can enhance the strength of the Fe layer, which could bring in a higher heterogeneity between adjacent layers. Significant heterogeneity in microstructure between Cu and Fe layers is expected to produce considerable mechanical incompatibility and synergetic deformation behaviors during deformation [5,14].

3.2. Mechanical behaviors

Fig. 3(a) presents the engineering stress–strain curves of three HS layered materials along with their individual Cu and Fe counterparts which were prepared by polishing away other layers. The freestanding CG Cu film exhibits good ductility but low strength, while the EG Fe film has higher yield stress but becomes unstable soon after yielding. However, when the CG Cu and EG Fe films are combined into heterogeneous layered materials, all HS layered materials demonstrate a significant balance of strength and ductility. Fig. 3(b) compares the corresponding true stress-strain curves vs strain-hardening rate curves. The strain hardening rate improves with decreasing interface spacing, leading to good uniform elongation at a high-stress level.

Fig. 3(c) summarizes the variation of yield strength and uniform elongation with interface spacing and Table 1 summarizes the me-

Table 1
Mechanical properties of HS Cu-Fe layered materials and freestanding Cu and Fe films.

Sample	Yield strength (MPa)	Ultimate strength (MPa)	Uniform elongation (%)	$P_{\Delta\sigma}$ (%)
A5 sample	321 ± 8	369 ± 11	9.2 ± 1.3	3.5
A17 sample	329 ± 9	385 ± 11	12.1 ± 1.8	6.1
A65 sample	346 ± 11	406 ± 12	13.9 ± 2.3	11.6
Cu 300 °C 2 h	127 ± 5	218 ± 8	25.9 ± 4.6	–
Fe 300 °C 2 h	494 ± 20	605 ± 22	2.8 ± 0.2	–

$P_{\Delta\sigma}$: Index of extra strengthening.

chanical properties of three-layered materials and their individual Cu and Fe counterparts. Here, a parameter $P_{\Delta\sigma}$ is defined to evaluate the extra strengthening, which is expressed by

$$P_{\Delta\sigma} = \left(\sigma_y - \sigma_{y,ROM}\right)/\sigma_{y,ROM} \times 100 \% \tag{1}$$

where σ_y is the experimental yield strength and $\sigma_{y,ROM}$ is the predicted yield strength by rule of mixture (ROM) theory [1]. Remarkably, the yield stress of A5, A17, and A65 samples surpasses the predicted value based on the ROM, indicating extra strengthening resulting from the HS layered structure, and the extra strengthening becomes more pronounced with increasing layer number (i.e., decreasing interface spacing), resulting in enhanced yield strength. The extra strengthening and higher strain hardening rate suggest
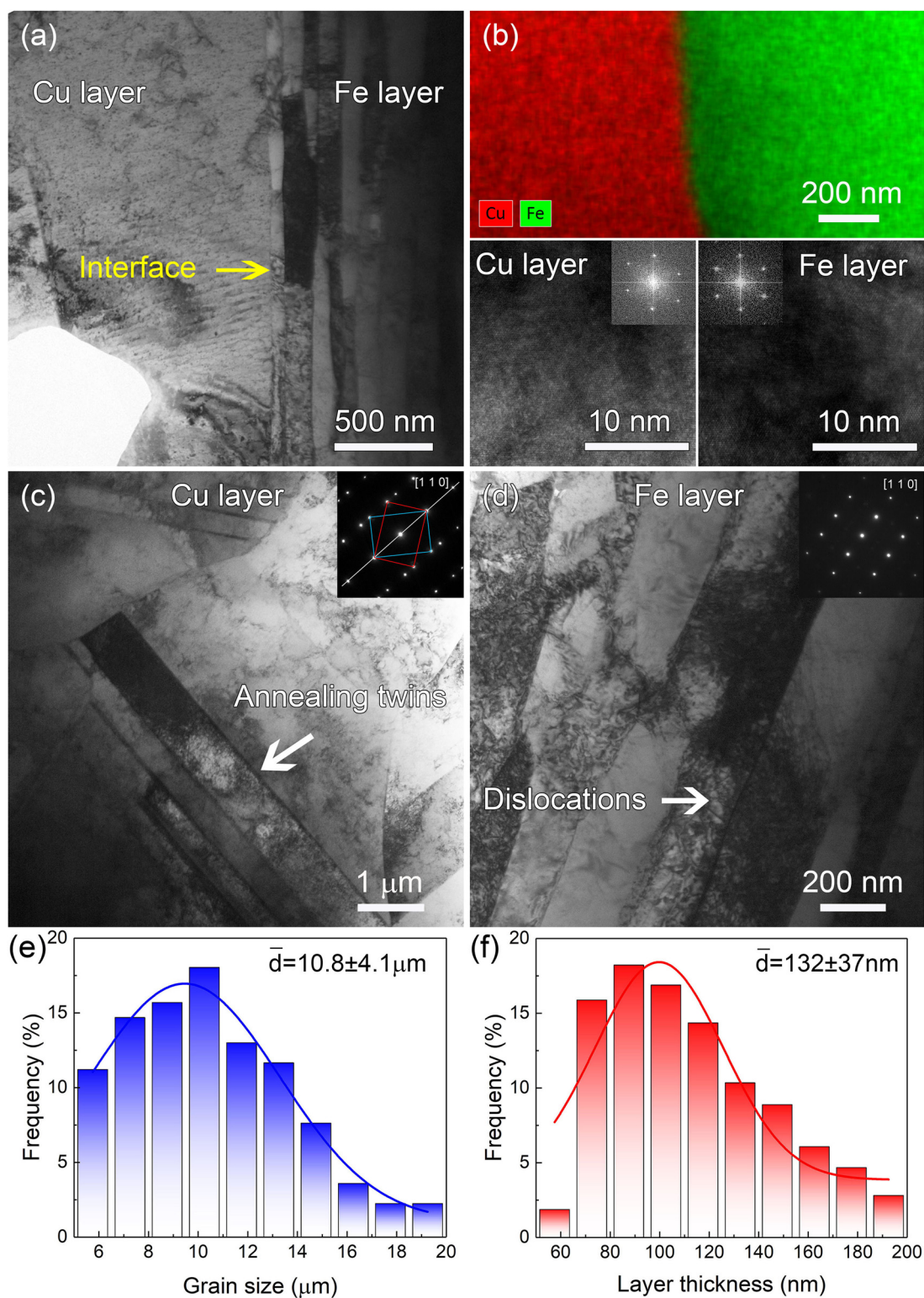
Fig. 2. Representative TEM images showing the microstructure of the A65 sample before the tensile test. (a) The overall morphology of Cu-Fe layered material. (b) EDS mapping showing the interface and high-resolution TEM revealing atoms of Cu (at low left position) and Fe (at low right position). (c) Equiaxed grains with annealing twins in the Cu layer. (d) Elongated grains with dislocated substructures in the Fe layer. (e) Grain size distribution in Cu layer. (f) Layer thickness distribution in Fe layer.
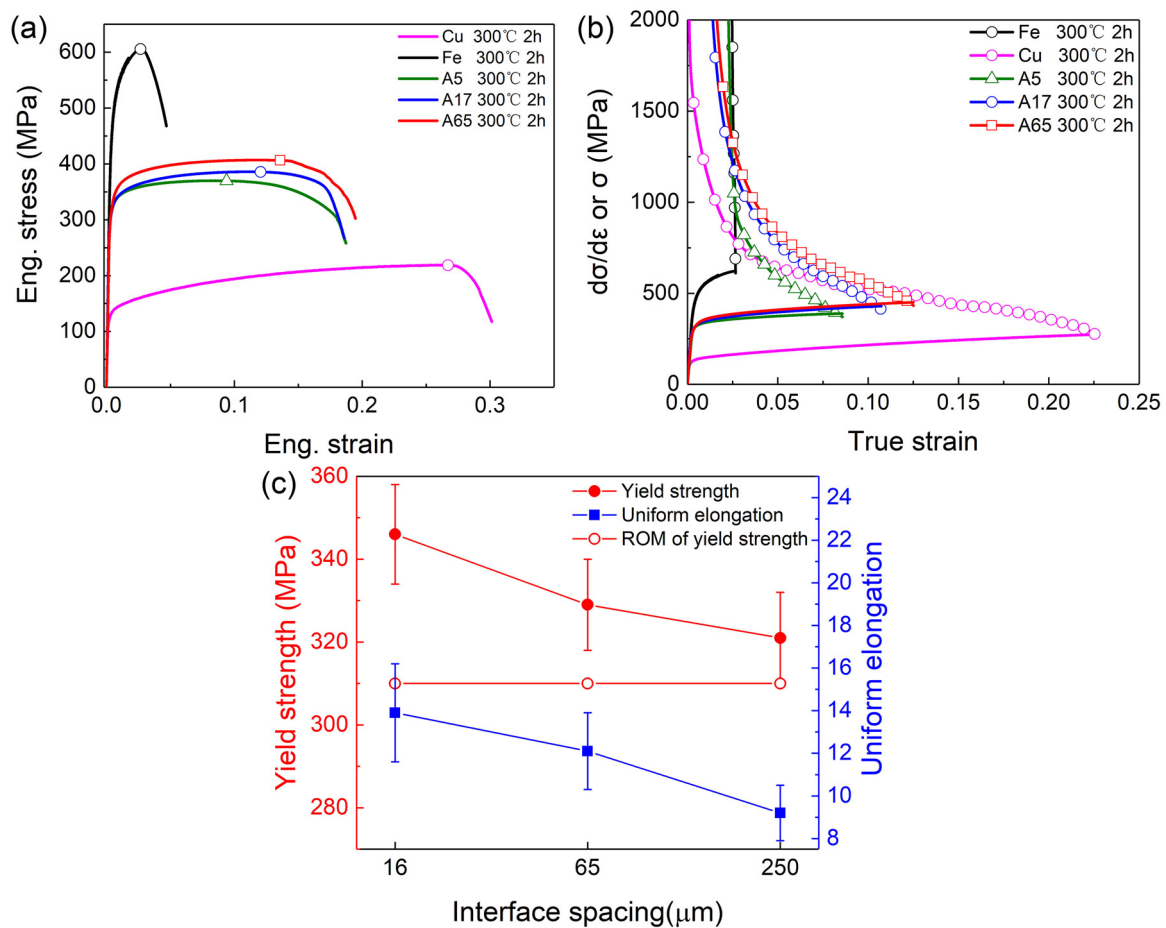
Fig. 3. Tensile behavior of three HS layered samples and freestanding Cu and Fe sheets. (a) Engineering stress–strain curves. (b) True stress–strain curves and strain-hardening rate curves. (c) Yield strength and uniform elongation plotted as a function of interface spacing.

that interface spacing contributes significantly to the strengthening and strain hardening capacity of the HS Cu-Fe layered materials.

3.3. Generation of GNDs

To elucidate the mechanisms responsible for the strengthening and strain hardening induced by interfaces, we conducted detailed analyses of the deformation behaviors in the vicinity of interfaces by using EBSD and TEM. Based on EBSD data, the kernel average misorientation (KAM) method was used to determine the local misorientation. The GND density was then calculated by $\rho_{GND} = 2\theta/\mu b$, where θ represents the local misorientation, b is the magnitude of Burger's vector (0.255 nm for Cu and 0.248 nm for Fe), and μ is the unit length of the point (50 nm in this study). Furthermore, the gradient in GND density was estimated using the conventional strain gradient theory [32,33]. Finally, to obtain the averaged GND density, the whole map was separated into several thin bars parallel to the interfaces to calculate the averaged GND density (Fig. 4). This method can minimize the errors caused by grain boundaries.

Fig. 4 shows the averaged GND density distributions of three layered samples at a tensile strain of ~1%, which are displayed as white squares and round dots in the Fe and Cu layers, respectively. The Cu layer exhibits a lower average GND density ($\sim 5.0 \times 10^{14}/m^2$) than the Fe layer ($\sim 17.6 \times 10^{14}/m^2$). Notably, a higher density of GNDs accumulates near the interfaces in all layered samples, forming a gradient distribution (Fig. 4(a–c)). Fig. 4(d)

is the enlarged view of the rectangle area in Fig. 4(b), the numbers under A, B, and C denote the GND densities at these points. It shows that the GND density at the layer interface is significantly higher than that at high-angle grain boundaries (HAGBs) on the Cu side, which suggests that the deformation in the region near the layer interface is more inhomogeneous, leading to higher GND density. In our previous work, the zone with a strain gradient was defined as IAZ [31], and later redefined as HBAR [13]. Due to the formation mechanism of strain gradient and GND density gradient [13], the width of the GND density gradient is identical to the strain gradient. So, in this study, the zones with GNDs density gradient can be regarded as another pattern of HBAR. The width of HBAR is taken as the distance from the interface to the place where the GND density gradient disappears. From Fig. 4, the widths of HBARs in Cu and Fe layers are ~5 μm and ~4 μm, respectively, giving the total HBAR width for Cu-Fe layered material ~9 μm. Based on the total thickness and number of HBARs in the A5, A17, and A65 layered materials, the volume fraction of HBAR in each layered material can be estimated as 3.6%, 14.4%, and 57.6%, respectively.

To investigate the evolution of GND density, the A65 samples were subjected to interrupted tensile testing at various strains, and the results are presented in Fig. 5. As anticipated, the GND density in both Cu and Fe layers increased with increasing tensile strain. Specifically, the averaged GND density in the Cu layer increases from $4.2 \times 10^{14}/m^2$ at the initial stage to $14.3 \times 10^{14}/m^2$ at a tensile strain of 8%. In contrast, a slight increment in GND den-
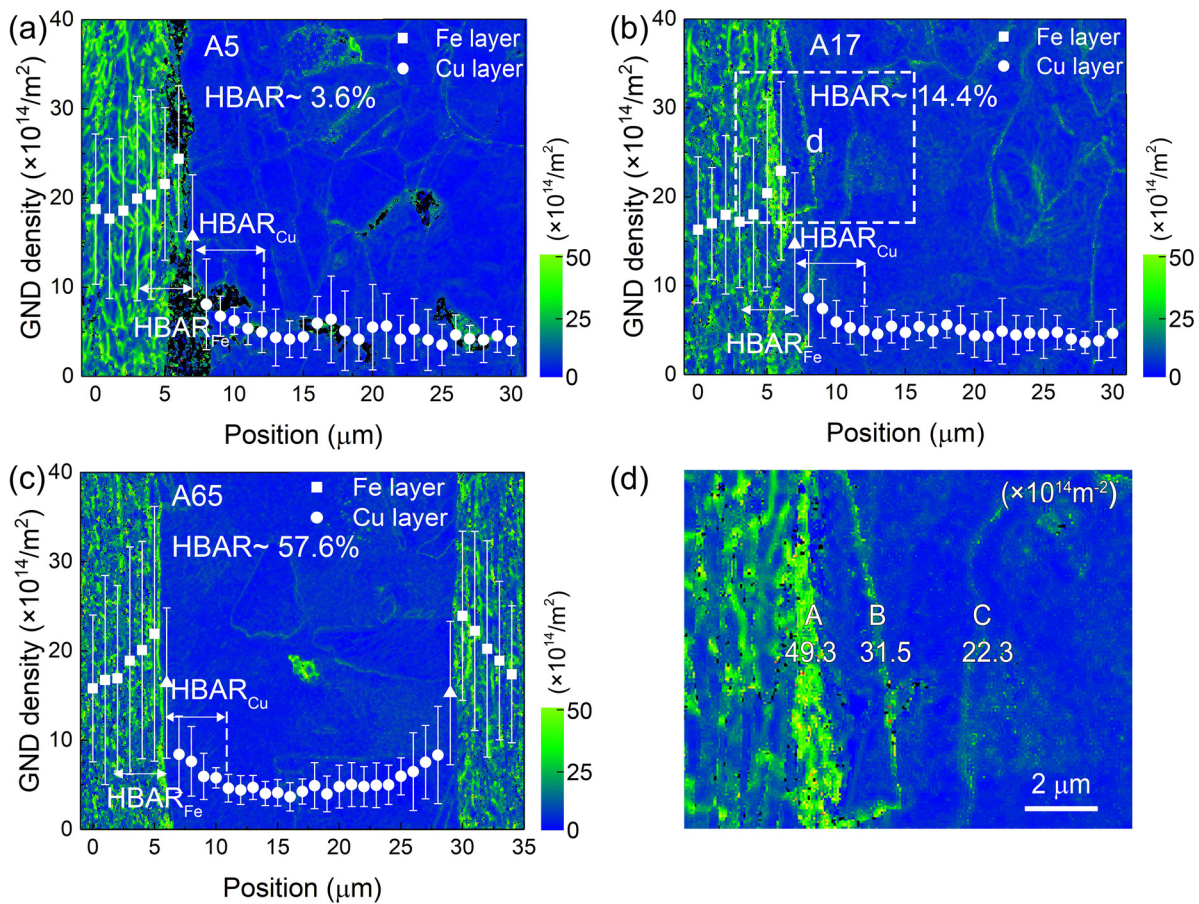
Fig. 4. Averaged GND density mapping based on EBSD data. (a) A5, (b) A17, and (c) A65 samples at the tensile strain of ∼1%. (d) Enlarged view of the white rectangle area in (b).

sity is observed in the Fe layers, ranging from $17.2 \times 10^{14}/\text{m}^2$ to $20.3 \times 10^{14}/\text{m}^2$. It suggests that the Cu layer accommodates more strain during tension, suggesting the occurrence of strain partitioning between the Cu and Fe layers.

Fig. 6 shows representative TEM images of the deformed structure near the interface at the point of tensile fracture. In comparison to the undeformed sample, a high density of dislocations is observed in the Cu layer after tension, some of them form dislocation arrays in the vicinity of the interface, as seen in Fig. 6(a). In the Fe layer, both dislocation tangles and arrays are observed near interfaces (Fig. 6(b)). If the dislocations in arrays are generated from the same dislocation source and have the same Burgers vector, they are GNDs that can produce long-range back stress to strengthen layered materials. HRTEM images and corresponding inverse fast Fourier transform (IFFT) images in Fig. 6(c, d) also demonstrate that dense dislocations are arrayed at interfaces. An enlarged view of Fig. 6(c) is shown in Fig. S3, we can clearly see the atoms in the figure, which confirms the reliability of the HRTEM image. These findings suggest that the Cu-Fe interface can serve as an important source for dislocations, thus facilitating improved strain hardening [34,35].

4. Discussion

The experimental results shown in Fig. 3 indicated that the strength-ductility combination of HS Cu-Fe layered materials improves with decreasing interface spacing. Previous investigations [3,10,13,15,24,31] have demonstrated that HBAR and GNDs play

crucial roles in enhancing the mechanical properties of different HS materials. Here, the mechanisms for enhancing the strength-ductility synergy of the HS Cu-Fe layered materials are discussed as follows.

4.1. Strain partitioning and interfacial strain gradient

The difference in the mechanical properties between the Cu and Fe layers can lead to heterogeneous deformation and synergistic constraints during the loading process [10–12,15,34]. The heterogeneous plastic deformation between layers can be reflected by the lateral profile of the specimen. Fig. 7(a1–c1) shows the 2D lateral surface height profile contours of three HS layered materials at 8% strain, and Fig. 7(a2–c2) displays the measurement data. Black and blue dots identify the locations of interfaces. All the results exhibit height differences between adjacent layers, and the degree of height difference $\bar{H}$ decreases with increasing interface number, showing more compatible deformation among the layers.

The height disparity observed in the Cu and Fe layers is due to their different lateral shrinkage extent. There is a report showing that this occurrence is attributed in part to the variation in Poisson's ratio and textures [36]. However, as illustrated in Fig. 7(a), the height difference between the Cu and Fe layers can be as high as ∼4 μm, such a substantial difference between layers cannot be attributed to the texture or Poisson's ratio alone. In the current case, the strain partitioning is considered as the main contributor to the lateral height disparity [2,34]. In Fig. 7(a), the Cu layer exhibits a higher plastic deformation capacity than that of the Fe
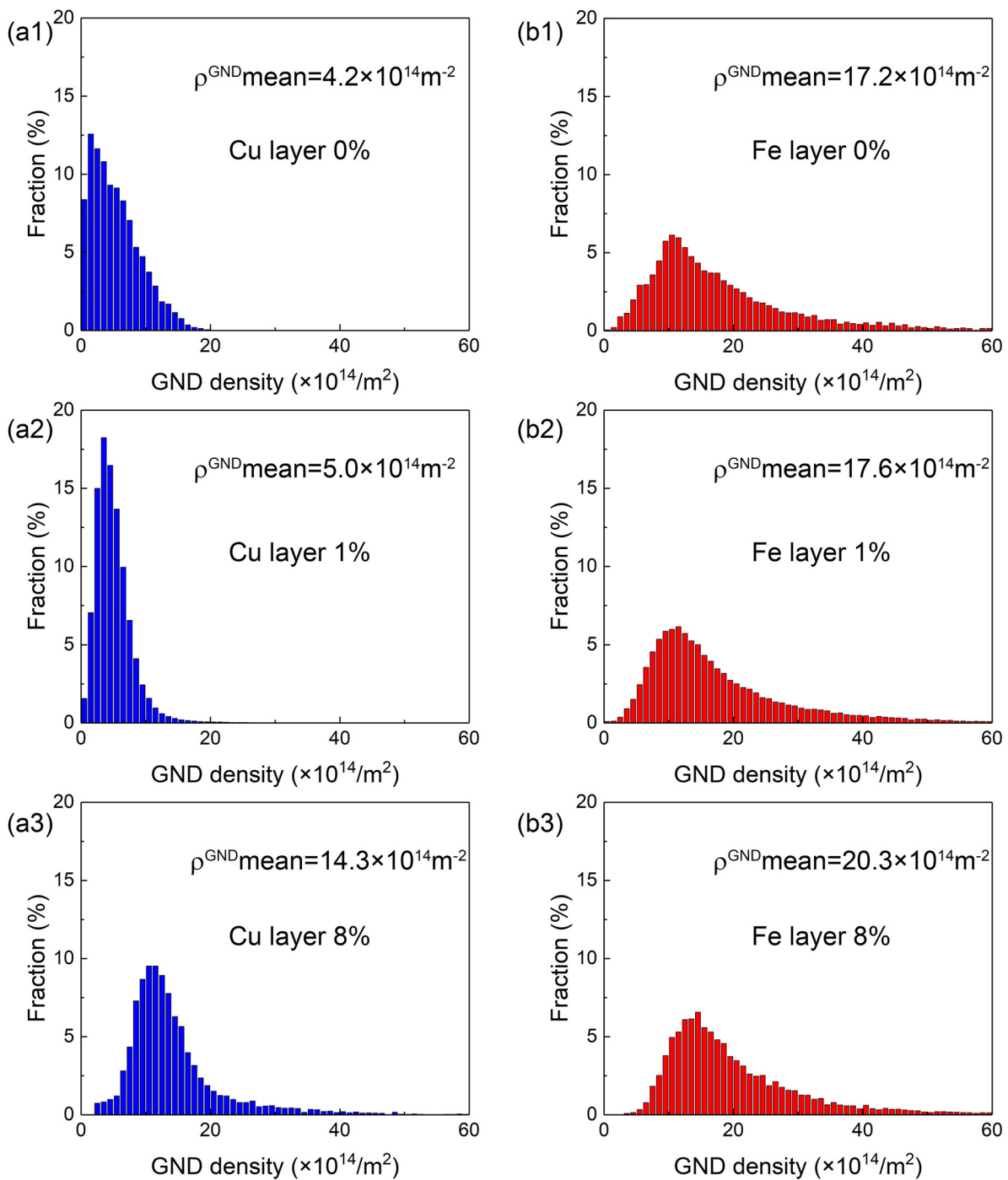
Fig. 5. Histogram distribution of GND density in A65 sample. (a) Cu and (b) Fe layers at varying interrupted tensile strains: (1) 0%. (2) ~1%. (3) ~8%.

layer, causing the Cu layers to bear more deformation and have more significant lateral shrinkage than the Fe layers. This marked difference in deformation results in a synergistic constraint between adjacent layers, which transforms the uniaxial stress state in each layer into a multiaxial stress state. Consequently, more dislocation slip systems are activated in each layer, resulting in improved strain hardening ability and delayed early plastic instability in the Fe layer. The multiaxial stress state is a cause of strain banding observed in the previous studies [37–40], which is also considered as reason for improving the ductility of HS layered materials.

Interestingly, a continuous transition in the lateral height of adjacent layers is observed in Fig. 7, indicating that strain partitioning is accompanied by a strain gradient at the layer interface. The zone with interfacial strain gradient is defined as HBAR. The existence of HBAR effectively accommodates the inhomogeneous deformation of the layers, and benefits strain hardening by accumulating GNDs. Additionally, the lateral height disparity between Cu and Fe layers becomes smaller with increasing layer number. Fig. 7(c2) demonstrates that the deformation ability of the Fe layer is comparable to that of the Cu layer in the A65 sample. It means that better compatibility in deformation can be obtained by in-
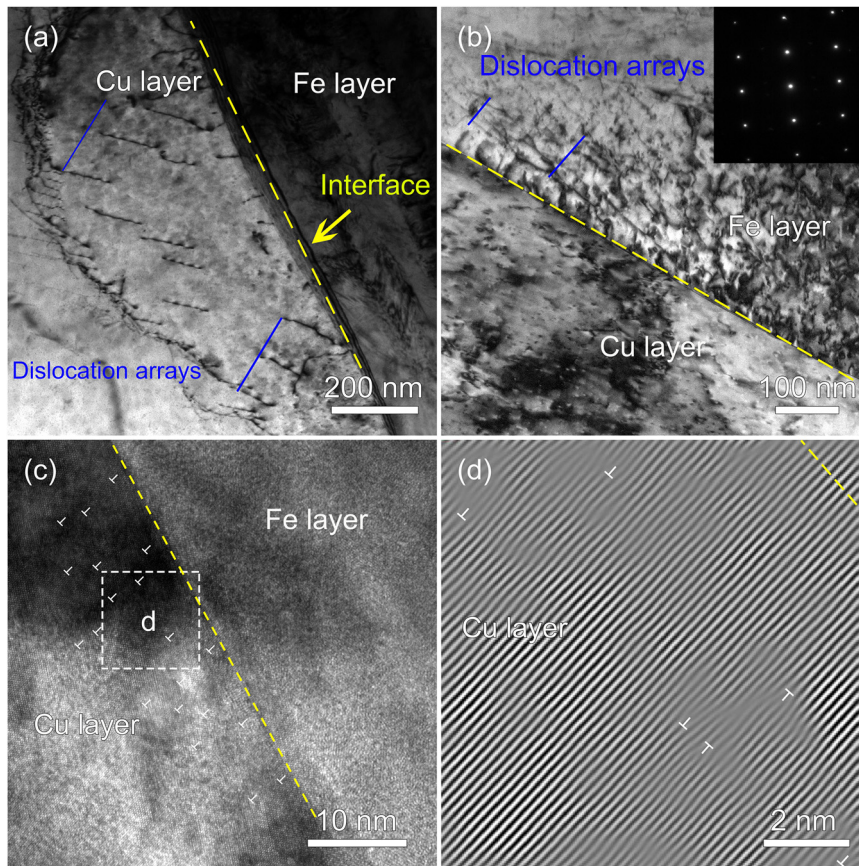
Fig. 6. Representative TEM images of the deformed structure near the interface at fractured tensile strain. Dense defects blocked/entangled in (a) Cu and (b) Fe layer near interface. (c) High-resolution TEM image near interface. (d) Dislocations stored in the Cu layer. Yellow dotted lines represent interfaces.

creasing layers. Since the interfacial strain gradient covers a relatively wide area respective to the decreased spacing, the deformation among the layers becomes more homogeneous. The strain delocalization and improved strain hardening ultimately lead to a better uniform elongation of the HS layered materials, as demonstrated in Fig. 3(a).

Fig. 7(a3–c3) depicts the lateral height gradient ($\overline{|HG|}$) distribution of the three samples, which are calculated by the derivative of lateral height in Fig. 7(a2–c2). The concept of "height gradient" mentioned here is different from "strain gradient". The height gradient is obtained by taking the derivative of the final lateral height, while the strain gradient represents the continuous difference in the strain component along the direction perpendicular to the layer interface. Here, $\overline{|HG|}$ reflects the level of strain partitioning between layers. The HBAR serves as a bridge for strain partitioning among different layers. The maximum values of $\overline{|HG|}$ are found to be located at or near the interface, indicating that the strain gradient at the interface is the highest. As a result, deformation inhomogeneity at the interface is the most severe and strain delocalization easily occurs. However, as the number of interfaces increases, the HBARs approach each other and even overlap, thus preventing strain localization and significantly reducing the value of $\overline{|HG|}$ at the interfaces. In other words, the synergistic deformation between layers is enhanced by decreasing layer spacing, fundamentally due to the overlap of interfacial strain gradient area (i.e., HBAR).

The interfacial strain gradient is formed through the generation and accumulation of GNDs [10–12,22,41,42]. Fig. 8(a) illustrates the distributions of GND density across two interfaces at tensile strains

of 0%, 1%, and 8%. Without deformation, the GND density distribution in each layer is nearly uniform, and Fe layers have a relatively higher initial GND density than that of the Cu layer due to its deformed microstructure. At an applied strain of 1%, GNDs accumulate near the interface, forming a GND density gradient. Continuously increasing strain results in a higher gradient of GND density near the interfaces, indicating enhanced deformation inhomogeneity between the adjacent layers. However, the width of the GND density gradient remains constant ($\sim$5 μm in the Cu layer).

Fig. 8(b) shows the increases in GND density from a strain of 0% to 1% and 1% to 8%. Both the Cu and Fe layers exhibit substantial increases in the GND density, while the increment in the Fe layer is relatively low. Notably, the regions near the interfaces have higher increments in GND density than the layer interior, indicating the strain gradient near the interface with loading strain. Here, the region containing the GND density gradient can be defined as the HBAR, which maintains a constant width during deformation [31,41]. As previously discussed, GND accumulation near the interface and interfacial strain gradient result from strain partitioning. Thus, HBAR is formed at the onset of strain partitioning. In addition to accommodating heterogeneous deformation, GNDs play an important role in strain hardening, which is known as HDI strain hardening [26].

4.2. Extra strengthening from HBAR

Besides strain hardening, extra strengthening can be also achieved from HBAR [13,31,43]. The accumulation of GNDs can impede the movement of mobile dislocations, resulting in Taylor-type
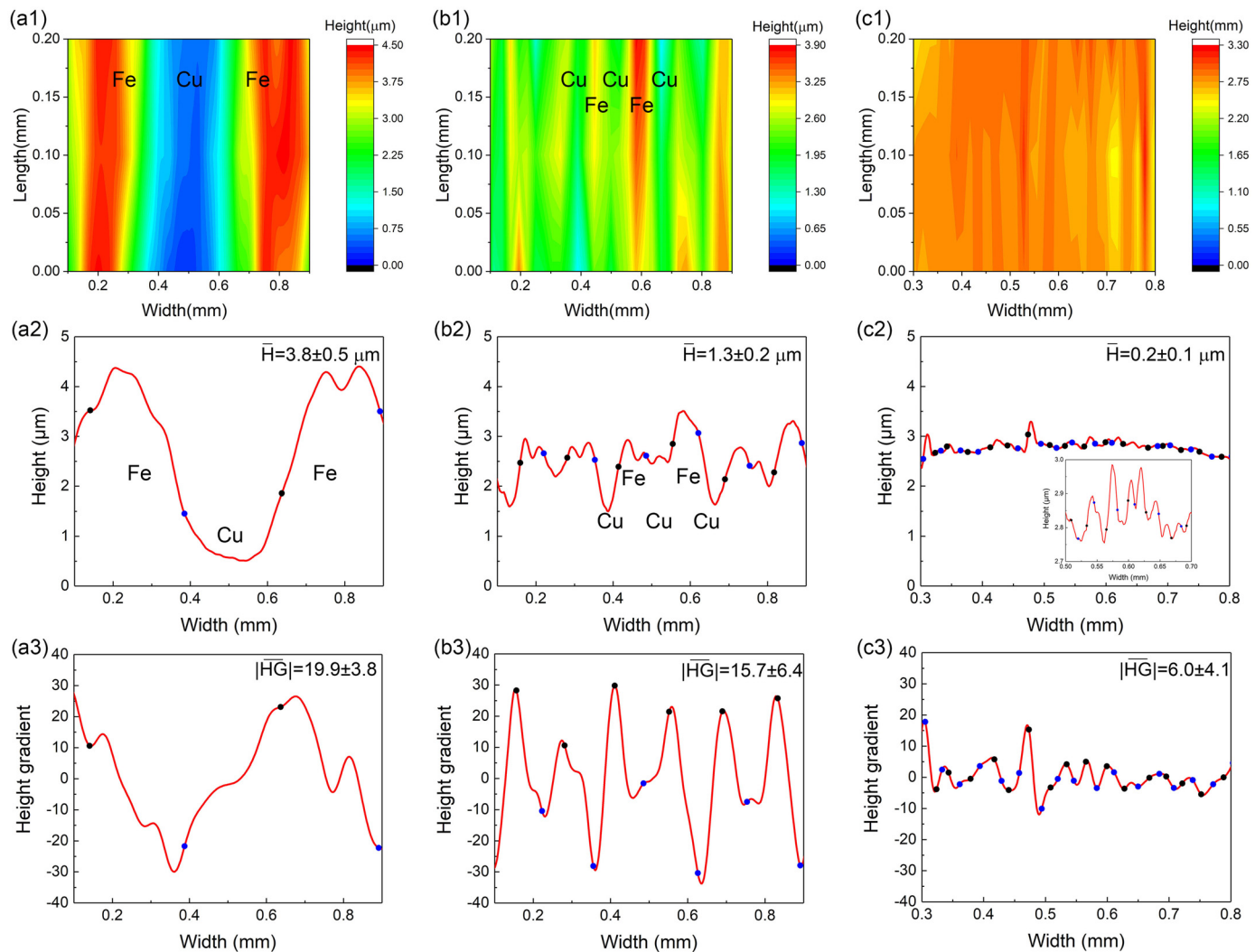
Fig. 7. Lateral surface height profile of three HS layered materials at the strain of 8%. (a1–c1) Contour plot of A5, A17, and A65 samples. (a2–c2) Contour line of A5, A17, and A65 samples. (a3–c3) Lateral height gradient calculated by contour line of A5, A17, and A65 samples. All dots are the locations of interfaces.

strengthening. Additionally, the accumulation of GNDs during tension can induce long-range internal stress known as HDI stress, which can further strengthen HS-layered materials. Therefore, the strengthening effect due to GND accumulation increases as the HBAR fraction increases. The extra strengthening effect for the HS layered materials is summarized in Fig. 9, by collecting data from Refs. [24,31,44,45]. In Fig. 9, $P_{\Delta\sigma}$ is the extra strengthening effect defined in Eq. (1), and the HBAR fraction is calculated by dividing the HBAR width by the total sample thickness. It is seen that the extra strengthening increases gradually with increasing the HBAR fraction. Notably, when the interface spacing decreases to the point where two adjacent HBARs overlap, it leaves insufficient space for dislocation accumulation, thereby contrarily weakening the strain-hardening ability [31]. In addition, the amplitude of the strain gradient would be reduced, which may result in a decrease in the density of GNDs and subsequently weaken the strength-ductility synergy [46]. As a result, it becomes difficult to simultaneously increase the strength and ductility. Thus, a higher HBAR fraction can obtain better strength-ductility synergy until two HBARs overlap (i.e., HBAR fraction is 100%).

Apart from the HBAR, increasing the interlayer heterogeneity can also improve the extra strengthening effect in HS-layered ma-

terials. This prolongs the elastic-plastic stage and enlarges the strain gradient between layers, leading to a greater accumulation of GNDs at the interface, thus producing a stronger extra strengthening [29]. However, excessive interlayer heterogeneity will increase the difficulty of synergetic deformation between layers and easily produce discontinuity across the interface. Therefore, tuning interlayer heterogeneity to build appropriate HBAR and strain partitioning among HS layers should be carried out to pursue a better strength-ductility synergy in layered materials.

5. Conclusions

In this study, we fabricated three HS layered materials using ARB and annealing treatment and investigated the deformation behaviors of Cu-Fe layered materials by tensile test, microstructure observation, and height profile measurement. The main conclusions are summarized as follows:

(1) In the HS layered material, the Cu layer is characterized by a CG microstructure with low dislocation density, while the Fe layer is an elongated nano-grained microstructure with high dislocation density. This heterogeneity in microstructure produces
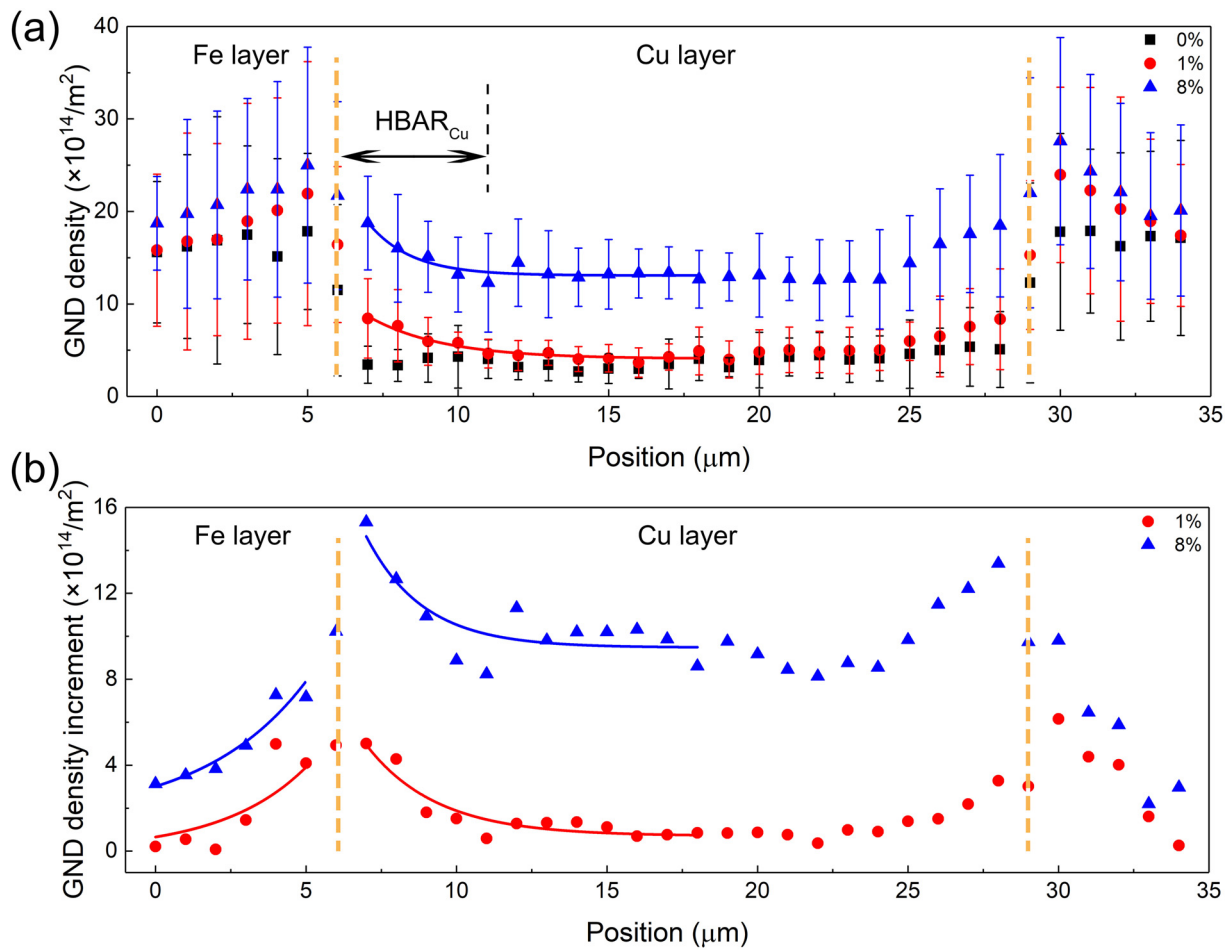
Fig. 8. Evolution of averaged GND density in the A65 sample based on EBSD data. (a) Distribution of averaged GND density at different strains. (b) Distribution of averaged GND density increment at different strains. The green dotted lines represent interfaces.
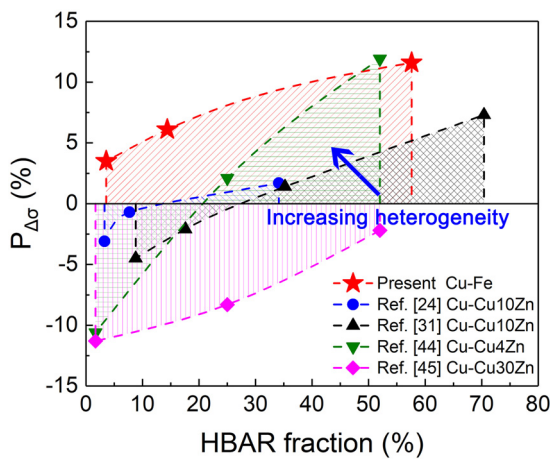

Fig. 9. Extra strengthening effect in layered materials with different HBAR fractions.

mechanical incompatibility and synergetic plastic deformation during tensile test.

(2) During deformation, mutual constraint and strain partitioning between adjacent layers lead to GNDs accumulation near the interface to accommodate the strain gradient and form HBARs, promoting strain hardening ability of HS layered materials and relieving strain localization at the interface. More interfaces can

induce more GND accumulation, which enhances the activation of HBARs and improves the synergetic deformation ability of HS-layered materials.

(3) The strength-ductility combination in layered materials is increased with increasing the HBAR fraction, due to higher GND density and corresponding enhanced HDI strengthening and hardening by GND density gradient.

Declaration of Competing Interest

The authors declare that they have no known competing financial interests or personal relationships that could have appeared to influence the work reported in this paper.

Acknowledgements

Supplementary materials

Supplementary material associated with this article can be found, in the online version, at doi:10.1016/j.jmst.2023.09.027.

References

[1] X.L. Wu, P. Jiang, L. Chen, J.F. Zhang, F.P. Yuan, Y.T. Zhu, Mater. Res. Lett. 2 (2014) 185–191.
[2] X. Wu, P. Jiang, L. Chen, F. Yuan, Y.T. Zhu, Proc. Natl. Acad. Sci. U. S. A. 111 (2014) 7197–7201.
[3] M. Yang, Y. Pan, F. Yuan, Y. Zhu, X. Wu, Mater. Res. Lett. 4 (2016) 145–151.
[4] F.J. Guo, Y.F. Wang, M.S. Wang, Q. He, H. Ran, C.X. Huang, Y.T. Zhu, Mater. Sci. Eng. A 782 (2020) 139256.
[5] T.H. Fang, W.L. Li, N.R. Tao, K. Lu, Science 331 (2011) 1587–1590.
[6] K. Lu, Science 345 (2014) 1455–1456.
[7] Y.F. Wang, C.X. Huang, M.S. Wang, Y.S. Li, Y.T. Zhu, Scr. Mater. 150 (2018) 22–25.
[8] X. Wu, Y. Zhu, K. Lu, Scr. Mater. 186 (2020) 321–325.
[9] X.T. Fang, G.Z. He, C. Zheng, X.L. Ma, D. Kaoumi, Y.S. Li, Y.T. Zhu, Acta Mater. 186 (2020) 644–655.
[10] X. Wu, Y. Zhu, Mater. Res. Lett. 5 (2017) 527–532.
[11] E. Ma, T. Zhu, Mater. Today 20 (2017) 323–331.
[12] Y. Zhu, K. Ameyama, P.M. Anderson, I.J. Beyerlein, H. Gao, H.S. Kim, E. Lavernia, S. Mathaudhu, H. Mughrabi, R.O. Ritchie, N. Tsuji, X. Zhang, X. Wu, Mater. Res. Lett. 9 (2021) 1–31.
[13] Y. Zhu, X. Wu, Prog. Mater. Sci. 131 (2023) 101019.
[14] Y. Wang, M. Chen, F. Zhou, E. Ma, Nature 419 (2002) 912–915.
[15] M.S. Wang, F.J. Guo, Q. He, W.L. Su, H. Ran, Q. Chen, H.S. Kim, Q.Y. Wang, C.X. Huang, Mater. Sci. Eng. A 883 (2023) 145513.
[16] X. Wu, M. Yang, F. Yuan, G. Wu, Y. Wei, X. Huang, Y. Zhu, Proc. Natl. Acad. Sci. U. S. A. 112 (2015) 14501–14505.
[17] Z.K. Li, X.T. Fang, Y.F. Wang, P. Jiang, J.J. Wang, C.M. Liu, X.L. Wu, Y.T. Zhu, C.C. Koch, Mater. Sci. Eng. A 777 (2020) 139074.
[18] H.K. Park, K. Ameyama, J. Yoo, H. Hwang, H.S. Kim, Mater. Res. Lett. 6 (2018) 261–267.
[19] C. Sawangrat, S. Kato, D. Orlov, K. Ameyama, J. Mater. Sci. 49 (2014) 6579–6585.
[20] R.H. Wang, M.S. Wang, R.R. Jin, Y.F. Wang, M. Yi, Q.Y. Li, J. Li, K. Zhang, C.H. Sun, Y. Nie, C.X. Huang*, A.G. Kikos, X.D. Zhang, Adv. Sci. 10 (2023) 2207698.
[21] X.L. Ma, C.X. Huang, W.Z. Xu, H. Zhou, X.L. Wu, Y.T. Zhu, Scr. Mater. 103 (2015) 57–60.
[22] D. Li, G. Fan, X. Huang, D. Juul Jensen, K. Miao, C. Xu, L. Geng, Y. Zhang, T. Yu, Acta Mater. 206 (2021) 116627.
[23] M. Huang, G.H. Fan, L. Geng, G.J. Cao, Y. Du, H. Wu, T.T. Zhang, H.J. Kang, T.M. Wang, G.H. Du, H.L. Xie, Sci. Rep. 6 (2016) 38461.
[24] X. Ma, C. Huang, J. Moering, M. Ruppert, H.W. Höppel, M. Göken, J. Narayan, Y. Zhu, Acta Mater. 116 (2016) 43–52.
[25] M. Huang, C. Xu, G. Fan, E. Maawad, W. Gan, L. Geng, F. Lin, G. Tang, H. Wu, Y. Du, D. Li, K. Miao, T. Zhang, X. Yang, Y. Xia, G. Cao, H. Kang, T. Wang, T. Xiao, H. Xie, Acta Mater. 153 (2018) 235–249.
[26] Y. Zhu, X. Wu, Mater. Res. Lett. 7 (2019) 393–398.
[27] Y. Wang, Y. Zhu, Z. Yu, J. Zhao, Y. Wei, Acta Mater. 241 (2022) 118395.
[28] J. Kang, N.S. Pottore, H. Zhu, C.C. Tasan, Acta Mater. 254 (2023) 118985.
[29] Y.F. Wang, C.X. Huang, X.T. Fang, H.W. Höppel, M. Göken, Y.T. Zhu, Scr. Mater. 174 (2020) 19–23.
[30] Y. Wang, Y. Zhu, X. Wu, Y. Wei, C. Huang, Sci. China Mater. 64 (2021) 3114–3123.
[31] C.X. Huang, Y.F. Wang, X.L. Ma, S. Yin, H.W. Höppel, M. Göken, X.L. Wu, H.J. Gao, Y.T. Zhu, Mater. Today 21 (2018) 713–719.
[32] C.S. Han, H. Gao, Y. Huang, W.D. Nix, J. Mech. Phys. Solids 53 (2005) 1188–1203.
[33] L.P. Kubin, A. Mortensen, Scr. Mater. 48 (2003) 119–125.
[34] Y.F. Wang, M.S. Wang, X.T. Fang, F.J. Guo, H.Q. Liu, R.O. Scattergood, C.X. Huang, Y.T. Zhu, Int. J. Plast. 123 (2019) 196–207.
[35] M.F. Ashby, Philos. Mag. J. Theor. Exp. Appl. Phys. 21 (1970) 399–424.
[36] W.H. Chen, W.J. He, Z.J. Chen, B. Jiang, Q. Liu, Int. J. Plast. 133 (2020) 102806.
[37] Y.F. Wang, C.X. Huang, Q. He, F.J. Guo, M.S. Wang, L.Y. Song, Y.T. Zhu, Scr. Mater. 170 (2019) 76–80.
[38] Y. Wang, Y. Wei, Z. Zhao, H. Long, Z. Lin, F. Guo, Q. He, C. Huang, Y. Zhu, Int. J. Plast. 149 (2022) 103159.
[39] Y. Wang, F. Guo, Q. He, L. Song, M. Wang, A. Huang, Y. Li, C. Huang, Mater. Sci. Eng. A 752 (2019) 217–222.
[40] J. He, Y. Ma, D. Yan, S. Jiao, F. Yuan, X. Wu, Mater. Sci. Eng. A 726 (2018) 288–297.
[41] H. Zhou, C. Huang, X. Sha, L. Xiao, X. Ma, H.W. Höppel, M. Göken, X. Wu, K. Ameyama, X. Han, Y. Zhu, Mater. Res. Lett. 7 (2019) 376–382.
[42] H. Wu, G. Fan, Prog. Mater. Sci. 113 (2020) 100675.
[43] J. Zhao, B. Liu, Y. Wang, Y. Liang, J. Li, X. Zhang, Mech. Mater. 179 (2023) 104599.
[44] T. Wan, Z. Cheng, L. Bu, L. Lu, Scr. Mater. 201 (2021) 113975.
[45] Z. Cao, Z. Cheng, W. Xu, L. Lu, J. Mater. Sci. Technol. 103 (2022) 67–72.
[46] W.H. Chen, W.J. He, N.C. Luo, Y.Z. Tang, Z.J. Chen, B. Jiang, Mater. Sci. Eng. A 859 (2022) 144230.